Degradation Analysis of Pt/Nb–Ti4O7 as PEFC Cathode Catalysts with Controlled Arc Plasma-deposited Platinum Content

Yongbing Ma, Hirokata Kajima, Yuta Shimasaki, Takaaki Nagai, Teko W Napporn, Hiroaki Wada, Kazuyuki Kuroda, Yoshiyuki Kuroda, Akimitsu Ishihara, Shigenori Mitsushima

Electrochemistry
The Electrochemical Society of Japan
Received: March 7, 2022
Accepted: April 11, 2022
Published online: April 14, 2022
Issued: May 27, 2022
https://doi.org/10.5796/electrochemistry.22-00025
https://doi.org/10.50892/data.electrochemistry.19586680
Article
Electrochemistry, **90(5)**, 057004 (2022)

Degradation Analysis of Pt/Nb–Ti_4O_7 as PEFC Cathode Catalysts with Controlled Arc Plasma-deposited Platinum Content†

Yongbing MA,[a,§] Hirokata KAJIMA,[a] Yuta SHIMASAKI,[b] Takaaki NAGAI,[c,§§] Teko W. NAPPORN,[c,d] Hiroaki WADA,[b,e] Kazuyuki KURODA,[b,e] Yoshiyuki KURODA,[a,c,§§] Akimitsu ISHIHARA,[c,§§] and Shigenori MITSUSHIMA[a,c,*,§§]

[a] *Graduate School of Engineering Science, Yokohama National University, 79-5 Tokiwadai, Hodogaya-ku, Yokohama 240-8501, Japan*
[b] *Department of Applied Chemistry, Faculty of Science and Engineering, Waseda University, 3-4-1 Ohkubo, Shinjuku-ku, Tokyo 169-8555, Japan*
[c] *Advanced Chemical Energy Research Center, Institute of Advanced Sciences, Yokohama National University, 79-5 Tokiwadai, Hodogaya-ku, Yokohama 240-8501, Japan*
[d] *IC2MP UMR 7285 CNRS University of Poitiers, 4 rue Michel Brunet B27 TSA 51106 86073, Poitiers Cedex 09, France*
[e] *Kagami Memorial Research Institute for Materials Science and Technology, Waseda University, 2-8-26 Nishiwaseda, Shinjuku-ku, Tokyo 169-0051, Japan*

* *Corresponding author: mitsushima-shigenori-hp@ynu.ac.jp, Tel: +81-45-339-4020, Fax: +81-45-339-4024*

ABSTRACT

For polymer electrolyte fuel cell cathodes, highly durable supports are required to prevent catalyst degradation in supports. In this study, as model Pt catalysts, 2–10 wt% Pt was deposited on Magnéli-phase niobium-doped macroporous Ti_4O_7 (Nb–Ti_4O_7) mounted on glassy carbon rods using the coaxial arc plasma deposition method. The morphologies of 2, 5, and 10 wt% Pt catalysts showed the hemisphere fine particles, islands with ca. 1.4 nm diameter and ca. 2.4 nm thickness, and films with ca. 3.3 nm thickness, respectively. During start/stop accelerated durability tests (ADTs) of 5000 cycles following the Fuel Cell Commercialization Conference of Japan protocol, Pt was slightly agglomerated; consequently, the morphologies of the 2, 5, and 10 wt% Pt catalysts were island-like with 3.5 nm thickness, chain bead-like with 4 nm thickness, and film-like with 4 nm thickness, respectively. This slight agglomeration led to good durability during the ADTs. Herein, the oxygen reduction reaction (ORR) mass activity (MA) values at 0.9 V vs. reversible hydrogen electrode (RHE) of the 2, 5, and 10 wt% Pt catalysts were 79, 60, and 36 A g_{Pt}^{-1} after 5000 cycles ADT, respectively, which had declining ratios after 5000 cycles were 32 %, 17 %, and 0 %, respectively. The island-like and film-like Pt/Nb–Ti_4O_7 presented activity and durability comparable to a Pt/C catalyst, which was 42 A g_{Pt}^{-1} (0.9 V vs. RHE) with a 12 % of declining ratio after the ADTs. The durability of the MA suggested that the different affinity caused by different crystal faces led to the slight agglomeration of 2, 5, and 10 wt%_Pt/Nb–Ti_4O_7 catalysts. These catalysts showed electrochemical surface areas (ECSAs) of 36, 27, and 29 $m^2\,g^{-1}$ after the ADTs, with declining ratios as low as 20 %, 6 %, and 0 %, respectively. All Pt/Nb–Ti_4O_7 catalysts showed higher durability of the ECSAs than the Pt/C catalyst, which was 68 $m^2\,g^{-1}$ with a 30 % declining ratio after the ADT. Different from common Pt nanoparticle catalysts, which agglomerate into large spherical Pt particles, the slight agglomeration was caused by the interconnection of the deposits and supplemented by a limited increase in the diameter or thickness. The island-like morphology of Pt with a limited thickness presented both high durability and activity among the Pt/Oxide catalysts.

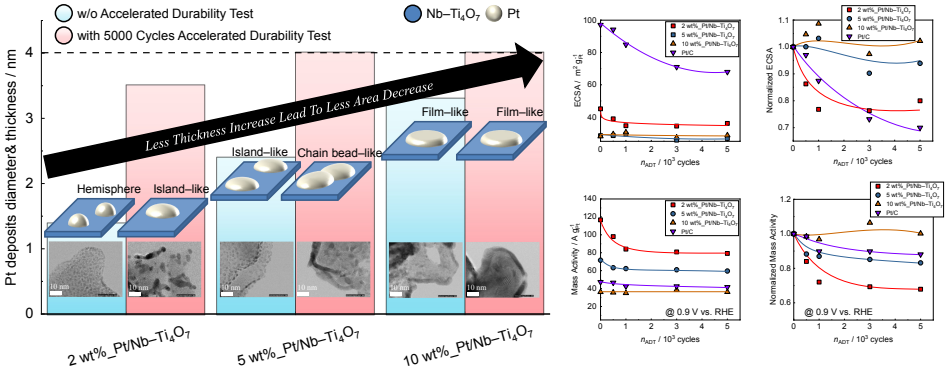

Keywords : Carbon Free ORR Catalysts, Polymer Electrolyte Fuel Cells, Carbon Free Catalysts Degradation Analysis, Pt Supported Cathode Catalysts

1. Introduction

Polymer electrolyte fuel cells (PEFCs) have generated considerable interest owing to their unique features, such as zero/low emission and high efficiency.[1] However, electrocatalysts durability is

†The content of this paper will be published by Yongbing MA as a PhD thesis at Yokohama National University in 2022.
§ECSJ Student Member
§§ECSJ Active Member
S. Mitsushima orcid.org/0000-0001-9955-2507

recognized as a limitation for their commercialization.[2–5] Carbon is a commonly used support for electrocatalysts in PEFCs owing to its numerous advantages, including high specific surface area, high conductivity, and commonly possessing functional groups that enable surface deposition of catalytically active materials.[6–11] However, the carbon supports used for PEFC cathodes undergo electrochemical corrosion during operation[12] caused by the oxidization of carbon under high potentials (standard electrode potential: 0.207 V vs. reversible hydrogen electrode (RHE)).[5] Thus, carbon-free cathode catalysts are urgently needed.

Recently, several conductive metal oxides have been reported as highly durable supports under high potentials for PEFCs. However, some are unstable in the highly acidic environment of the proton exchange membrane of PEFCs. Indium tin oxide,[13] TiO_2,[14] and Ti_6O_{11}[15] are stable in acidic environments. Reduced titanium oxides possessing Magnéli phase structures (Ti_nO_{2n-1}; $4 \leqq n \leqq 10$),[16,17] particularly Ti_4O_7, are some of the most interesting support materials for PEFC cathodes because their high conductivity values are similar to those of carbon materials[17] and they are high in acidic media.[18,19] Magnéli-phase Ti_4O_7 is synthesized by reducing the TiO_2 precursor by H_2 reduction,[20] metallothermic,[16] and carbothermal reduction.[21] However, it is difficult to maintain the large surface area using these high-temperature processes (approximately 1000 °C). We have previously reported a hydrothermal synthesis of Nb–doped TiO_2 nanoparticles for their application as PEFC cathode supports.[22] Their conductivity and surface area were negatively correlated because enhanced conductivity was achieved only by H_2 reduction at higher temperatures, which increased the agglomeration of primary particles, and thereby reduced the surface area. Utilizing its high conductivity and large surface area, Nb–doped/added TiO_x has also been extensively used as a support in PEFC cathodes.[23–26] We have also reported a templated synthesis of macroporous Magnéli-phase Ti_6O_{11} as a potential support for PEFC cathodes.[15] A highly ordered porous structure with a Ti_6O_{11} framework was obtained by the deposition of a TiO_2 precursor within a colloidal crystal template, followed by H_2 reduction. The templating process was advantageous for suppressing the agglomeration of the TiO_x framework during H_2 reduction at high temperatures (800 °C). However, the Brunauer–Emmett–Teller (BET) surface area of macroporous Ti_6O_{11} was only 11 $m^2\,g^{-1}$ owing to the agglomeration of the TiO_2 precursor units deposited outside of the template. Therefore, this synthetic method must be optimized to achieve both high conductivity and a large surface area.

From the aspect of durability and the oxygen reduction reaction (ORR) activity, oxide supports are expected to enhance both the mass and specific activities of Pt by strong metal support interaction (SMSI). Recently, Mukerjee et al. emphasized both metal-metal and metal-oxygen interactions to propose metal and metal oxide interactions.[27] Many studies have shown that the interaction between Pt and titanium-oxide-based supports enhance both the mass activity (MA) and durability of Pt.[18,24,26–34] In our previous study on a microporous Ti_6O_{11} support, Pt nanoparticles were deposited it using the coaxial arc plasma deposition (APD) method. Owing to the high energy applied for Pt vaporization, Pt nanoparticles deposited by APD possess unique properties, such as controllable particle size,[35,36] high activity,[37,38] and high durability.[38] In our study, the Pt nanoparticles deposited by APD on the macroporous Ti_6O_{11} presented a relatively high specific activity (SA) of 6.01 A m^{-2} at 0.9 V vs. RHE.[15] However, although the high durability of Pt/titanium-oxide-based catalysts have been commonly reported, the explanations of this property being better than those of Pt/C catalysts are typically the decreased oxidation of the titanium oxides supports and the SMSI between the supports and the metal. Moreover, the deterioration mechanism of the former catalyst has not been fully revealed until now.

To determine the mechanism of deterioration of Pt/titanium-oxide-based catalysts, herein, we studied the deterioration characteristics of Pt supported on a macroporous Nb-doped Ti_4O_7 (Nb–Ti_4O_7)[39] support in acidic media. The Pt deposition was performed by APD, wherein the number of arc plasma discharges was varied to obtain distinct Pt loading amounts as model Pt/Nb–Ti_4O_7 catalysts. Using the model catalysts, we examined the differences in the physical and electrochemical properties of Pt at different loadings by conducting accelerated durability tests (ADTs). The physical and electrochemical characteristics of each Pt loading and the degradation mechanism of the Pt/Nb–Ti_4O_7 synthesized using the APD method were analyzed.

2. Experimental

2.1 Materials

Tris(hydroxymethyl)aminomethane, (THAM, ACS reagent, ≥99.8 %, Sigma-Aldrich), tetraethyl orthosilicate, (TEOS, ≥99.0 %, Sigma-Aldrich), titanium tetrachloride ($TiCl_4$, 16–17 % as Ti, FUJIFILM Wako Pure Chemical Corporation), concentrated hydrochloric acid (HCl, 35.0–37.0 %, FUJIFILM Wako Pure Chemical Corporation), titanium(IV) tetrabutoxide ($C_{16}H_{36}O_4Ti$, TBOT, 97 %, Sigma-Aldrich), niobium(V) pentachloride ($NbCl_5$, 99 %, Sigma-Aldrich) were used for the preparation of macroporous Nb–TiO_2 in the experiments. Electrolytes were prepared using ultrapure water treated with Purelite (Organo Corporation) and perchloric acid ($HClO_4$, guaranteed reagent, FUJIFILM Wako Pure Chemical Corporation). Isopropanol ($(CH_3)_2CHOH$, guaranteed reagent, FUJIFILM Wako Pure Chemical Corporation), and Nafion® solution (5 % Nafion® dispersion solution DE521 CS type, FUJIFILM Wako Pure Chemical Corporation) were used to prepare the catalyst ink for the Pt/C catalyst. None of the reagents required additional purification.

2.2 Synthesis of macroporous Nb–Ti_4O_7

Macroporous Nb–Ti_4O_7 was synthesized by thermal H_2 reduction of macroporous Nb–TiO_2 in the presence of a silica template. Macroporous Nb–TiO_2 was prepared via seed-mediated templating based on a previous study.[40] A colloidal crystal template was synthesized according to previously reported methods.[41] Briefly, a dispersion of silica nanospheres was obtained by heating an aqueous solution of TEOS and THAM in 500 mL of deionized water (TEOS : THAM : H_2O = 45 : 1 : 2780, molar ratio) at 80 °C for 24 h. A part of the solution (seed nanospheres) was transferred into another aqueous solution containing THAM, followed by the addition of TEOS in the above-stated molar ratio. The newly added TEOS was consumed only by the particle growth of the seed nanospheres. The particle size is calculated using the following equation:

$$\left(\frac{\text{Diameter}_{\text{final}}}{\text{Diameter}_{\text{seed}}}\right)^3 - 1 = \frac{\text{Mass}_{\text{TEOS,added}}}{\text{Mass}_{\text{TEOS,seed}}} \quad (1)$$

The size of the silica nanospheres was maintained at 60 nm. After evaporating the solvent at 50 °C and a subsequent heating at 550 °C for 6 h, the colloidal crystal template was obtained.

A Ti-containing template was prepared by hydrolyzing $TiCl_4$ in the presence of the silica template. A $TiCl_4$ stock solution (2 M) was prepared by mixing $TiCl_4$ (2 mL), deionized water (7 mL), and conc. HCl (20 µL) over an ice bath. The stock solution was diluted with deionized water to prepare 15 mM $TiCl_4$ solution (33 mL). The colloidal crystal template (5.0 g) was added to the solution, and the mixture was kept at 70 °C for 1 h without stirring. The Ti-containing template was recovered by filtration, washed with deionized water, and calcined at 550 °C for 30 min.

TBOT (0.8 mL) and 0.2 M $NbCl_5$ (120 µL) were added to a mixture of water (28 mL) and conc. HCl (28 mL). The Nb/Ti molar

ratio was 0.01. The Ti-containing template (0.72 g) was added to the solution, which was subsequently transferred into a 100-cm^3 Teflon-lined stainless-steel autoclave. The autoclave was capped tightly and heated at 150 °C for 12 h. After cooling to 25 °C, the precipitate was centrifuged, washed several times with deionized water and ethanol, and dried under vacuum at 80 °C for 12 h.

Macroporous Nb–TiO_2 with the unremoved template was heated at 900 °C for 5 h in a tube furnace under H_2 flow (200 cm^3 min^{-1}) to reduce the Nb–TiO_2 framework transfer to Nb–Ti_4O_7 inside the template. The colloidal crystal template was removed by heating at 80 °C in aqueous 2 M NaOH for 2 h, followed by centrifugation, washing, and drying. Templates were also removed from Nb–TiO_2 without H_2 reduction to prepare macroporous Nb–TiO_2 for comparison with macroporous Nb–Ti_4O_7.

2.3 Preparation of Pt/Nb–Ti_4O_7 electrodes

Pt deposition on the surface of Nb–Ti_4O_7 mounted on a glassy carbon (GC) rod was achieved using the APD method based on our previous study.[15] First, 4 mg of Nb–Ti_4O_7 was suspended in 400 µL 1-hexanol (97 %, FUJIFILM Wako Pure Chemical Corporation), followed by sonication for 20 min to prepare a Nb–Ti_4O_7 ink. Subsequently, 10 µL Nb–Ti_4O_7 ink was dropped onto a GC rod ($\varphi = 5.2$ mm, Tokai Carbon Co., Ltd.), and dried at 60 °C for 1 h (denoted as Nb–Ti_4O_7/GC). Nb–Ti_4O_7/GC was placed in the vacuum chamber of model APD-S (ADVANCE RIKO, Inc.), and Pt was deposited under the following conditions: discharge voltage = 100 V, condenser capacity = 1080 µF, pulse frequency = 3 Hz, and chamber pressure = 6.7×10^{-3} Pa. The discharge energy was 5.4 J per pulse. As the deposition rate under these conditions was 0.035 nm per pulse (average of 3000 pulses), the number of pulses was set as 133 to deposit 2 wt% Pt relative to Nb–Ti_4O_7 mounted on the GC rod. Samples with Pt loadings of 2, 5, and 10 wt% were prepared by changing the number of pulses to 133, 332, and 663 shots, respectively (denoted as 2 wt%_Pt/Nb–Ti_4O_7, 5 wt%_Pt/Nb–Ti_4O_7, and 10 wt%_Pt/Nb–Ti_4O_7, respectively). The Pt loading amount for APD was confirmed in a previous study using by inductively coupled plasma atomic emission spectroscopy.[15] The Pt loading was adjusted based on the weight ratio of Nb–Ti_4O_7 on the GC rod. Pt could not be deposited uniformly inside the pores of Nb–Ti_4O_7 by APD because the deposition was in one direction. Therefore, the morphology of the deposited Pt was observed using a microscope.

Because the Pt/Nb–Ti_4O_7 catalysts could not be uniformly dispersed using by ultrasonication, Nafion® was not expected to be uniformly covered on their surfaces. To reduce the interference on the Pt surface, Nafion® was not used for the preparation of the Pt/Nb–Ti_4O_7/GC electrodes. A commercial Pt/C (TEC10E50E, Tanaka Kikinzoku Kogyo) catalyst was used for comparison. Pt/C was mounted on a GC rod using the same procedure as that for the preparation of Nb–Ti_4O_7/GC, except that Nafion® was dissolved in the ink to prevent the peeling of Pt/C from the GC rod. To reduce the interference by Nafion®, the amount of Nafion® added was halved based on the Fuel Cell Commercialization Conference of Japan (FCCJ) standard method.[42]

2.4 Physical characterization

Powder X-ray diffraction (XRD) patterns of the samples were recorded on a Rigaku Ultima IV diffractometer with CuKα1 radiation ($\lambda = 0.15406$ nm). The N_2 adsorption-desorption isotherm of macroporous Nb–Ti_4O_7 was measured using a MicrotracBEL BELSORP-mini Instrument at −196 °C. The electrical resistance of the macroporous Nb–Ti_4O_7 powder was measured using a cylindrical cell in which circular electrodes were placed on both top and bottom (Fig. S1a). The powdery sample was placed in the cylinder, and a pressure of up to 60 MPa was applied along the longitudinal direction. DC resistivity was measured using a Hioki RM3545 resistance meter. The conductivity (σ) is calculated as follows:

$$\sigma = \frac{t}{AR} \tag{2}$$

where t, A, and R are the thickness of the sample under a uniaxial pressure, the area of the circular electrode (0.196 cm^2), and the measured resistance, respectively. Scanning transmission electron microscopy (STEM) images were obtained using a Hitachi Cs-corrected STEM HD-2700 microscope at an accelerating voltage of 200 kV. X-ray photoelectron spectroscopy (XPS) was performed on the Al mono using a PHI5000 VersaProbe II instrument. A Gaussian–Lorentzian line shape with a Shirley background was used for electron binding energy and asymmetry analysis. The peak areas of the $4f_{7/2}$ and $4f_{5/2}$ components were fixed at 4 : 3, and a theoretical spin-orbit splitting of 3.33 eV was used in the analysis.[43] Photoemission spectra were calibrated against the C 1s peak, which was used as the internal standard, and the binding energy of C 1s was 284.8 eV. The spectra were deconvoluted into three fitted peak components, qualitatively and quantitatively, based on the reported peak position range.[44–49]

2.5 Electrochemical characterization

Electrochemical tests were performed using a glass three-electrode cell in a Toho Technical Research PS08 potentiostat. Aqueous 0.1 M $HClO_4$ (300 mL) was used as the electrolyte. A GC plate and RHE were used as the counter and reference electrodes, respectively. Before evaluating the ORR activity, cyclic voltammetry was performed from 0.2 to 1.2 V at a scan rate of 200 mV s^{-1} at 60 °C in 0.1 M $HClO_4$ under N_2 saturation for 200 cycles as a pre-treatment to obtain a clean surface.

ADT entailing potential scanning using a triangle wave with a potential scan rate of 500 mV s^{-1} from 1.0 to 1.5 V at 60 °C was conducted using the start/stop cycle test recommended by the FCCJ.[42]

Cyclic voltammograms (CVs) were recorded under pure nitrogen flow at 60 °C at a scan rate of 50 mV s^{-1} from 0.05 to 1.2 V to evaluate the electrochemically active surface area (ECSA) based on the mass of Pt. The ECSA of the Pt deposited on macroporous Nb–Ti_4O_7 was calculated from the difference between the average integrated charge of the hydrogen adsorption and desorption (Q_H) waves from 0.05 to 0.4 V in the CVs, and of the charging current of the electrical double layer estimated at 0.39–0.41 V. A conversion factor ($q_H = 0.21$ mC cm^{-2}) was applied for monolayer adsorption of hydrogen on the Pt surface was used to obtain the ECSA. Thus, the ECSA is calculated using the following equation:[50]

$$\mathrm{ECSA} = \frac{Q_H}{m \times q_H} \tag{3}$$

Here, m is the Pt loading mass. Cyclic voltammetry at a scan rate of 5 mV s^{-1} in the range of 0.2–1.2 V was performed in 0.1 M $HClO_4$ under oxygen bubbling for over 30 min prior to the measurement to evaluate the ORR current density as a function of potential. To obtain steady CVs, four voltammetric cycles were performed, and the last cycle was used for evaluation.

3. Results and Discussion

3.1 Physical characterization of macroporous Nb–Ti_4O_7 support

The XRD patterns of macroporous Nb–TiO_2 (post-template removal) and Nb–Ti_4O_7 are shown in Fig. 1. The former support consisted of anatase, rutile (major phase), and brookite phases, which is consistent with a previous report.[39] Peaks arising from segregated Nb species were not observed, suggesting that Nb was doped in the TiO_2 framework. After H_2 reduction, the crystal

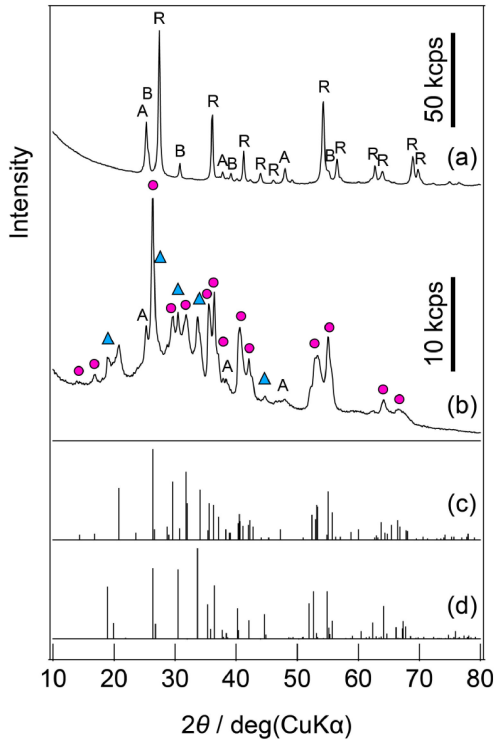

Figure 1. XRD patterns of (a) macroporous Nb–TiO_2 and (b) macroporous Nb–Ti_4O_7. Simulated diffraction peaks of (c) Ti_4O_7 (JCPDS 050-0787) and (d) γ-Ti_3O_5 (JCPDS 076-1066). Peaks due to rutile, anatase, and brookite are marked by R, A, B, respectively. Peaks due to Ti_4O_7 and γ-Ti_3O_5 are marked purple filled circles and blue filled triangles, respectively.

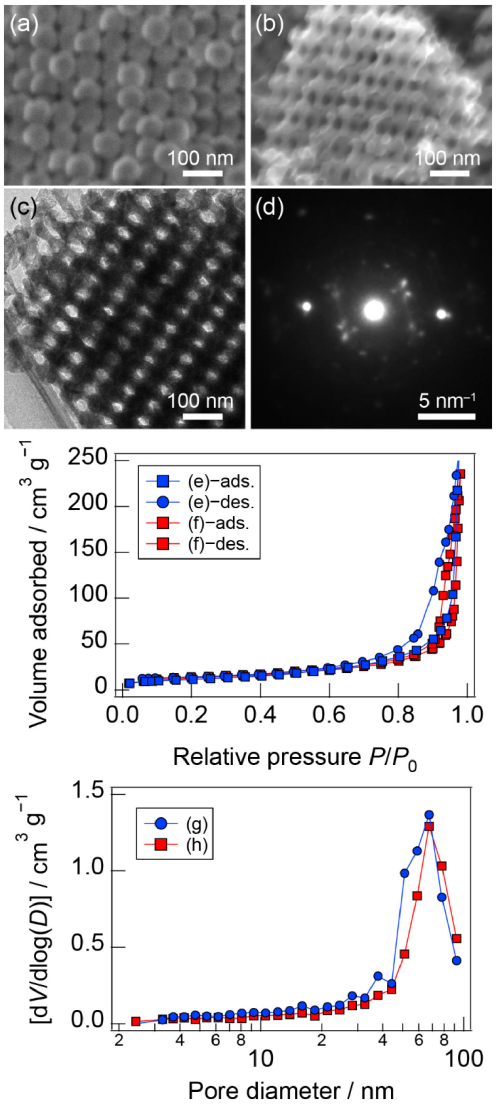

Figure 2. SEM images of (a) colloidal crystal template and (b) macroporous Nb–Ti_4O_7. (c) TEM image, (d) the corresponding selected area electron diffraction pattern, (e, f) N_2 adsorption-desorption isotherms, and (g, h) BJH pore size distribution curves of (e, g) macroporous Nb–TiO_2 and (f, h) macroporous Nb–Ti_4O_7.

structure of the TiO_2 framework changed to conductive Ti_4O_7 (major phase) and γ-Ti_3O_5 phases. Small peaks due to anatase TiO_2 remained, probably owing to insufficient reduction of the Nb–TiO_2 framework present deep inside the template. Peaks indicative of Nb species were not observed after reduction. Thus, we concluded that Nb was incorporated in the frameworks of Ti_4O_7, γ-Ti_3O_5, and anatase; further analyses are required to elucidate the conditions of Nb in the material.

Figure 2a shows the colloidal crystal template, indicating that the size of the silica nanospheres is uniformly controlled at 60 nm. The SEM and TEM images of macroporous Nb–Ti_4O_7 as shown in Figs. 2b and 2c indicated that a well-ordered macroporous structure is formed even after H_2 reduction, as shown in Figs. 2b and 2c. In contrast, in our previous study on macroporous Ti_6O_{11},[15] a well-ordered porous structure was observed only in part. In this research, the use of Ti-containing colloidal crystals contributed to the deposition of Nb–TiO_2 in the interstices of the silica nanospheres of the colloidal crystal template; therefore, the physically confined Nb–TiO_2 framework could be converted into the reduced phases without deformation of the nanostructure. The selected area electron diffraction of macroporous Nb–Ti_4O_7 is shown in Fig. 2d. The observation of a spot pattern, instead of a ring pattern, suggested that the framework consisted of single crystal-like large crystallites, which is advantageous for achieving high conductivity with low boundary resistance. The size of the mesopores was measured to be 60 nm.

The N_2 adsorption-desorption isotherms and the corresponding Barrett–Joyner–Halenda (BJH) pore size distribution curves of macroporous Nb–TiO_2 and Nb–Ti_4O_7 are shown in Figs. 2e–2h. The isotherms do not differ significantly, suggested that H_2 reduction marginally affects their macroporous structure. The BET surface area of macroporous Nb–Ti_4O_7 was 46 $m^2 g^{-1}$, which is considerably higher than those of macroporous Ti_6O_{11} (11 $m^2 g^{-1}$, determined in our previous study[15]) and other nanostructured Ti_4O_7.[18,19] The mean BJH pore size of macroporous Nb–Ti_4O_7 was 68 nm. The differences in the sizes measured by the different methods, which are caused the measured SEM and TEM images, not only including the pore diameters but also the diameters of the base of the spherical caps, which is inevitable owing to image limitation, therefore it is consistent with the pore sizes estimated from the SEM and TEM images.

The conductivity of macroporous Nb–Ti_4O_7 as a function of the uniaxial pressure is shown in Fig. S1b. The conductivity initially increased with the decrease in the sample thickness due to the uniaxial pressing and subsequently reached a constant value of 0.10 S cm^{-1} at 60 MPa. The initial filling rate of the sample in the measuring fixture was 7 %. Although the surface areas of the Nb–TiO_x nanoparticles from our previous study[22] and macroporous Nb–Ti_4O_7 were of similar orders, the latter had higher conductivity than had the former by two orders. Figure S2 summarizes the relationship between the conductivity and surface area of various reported

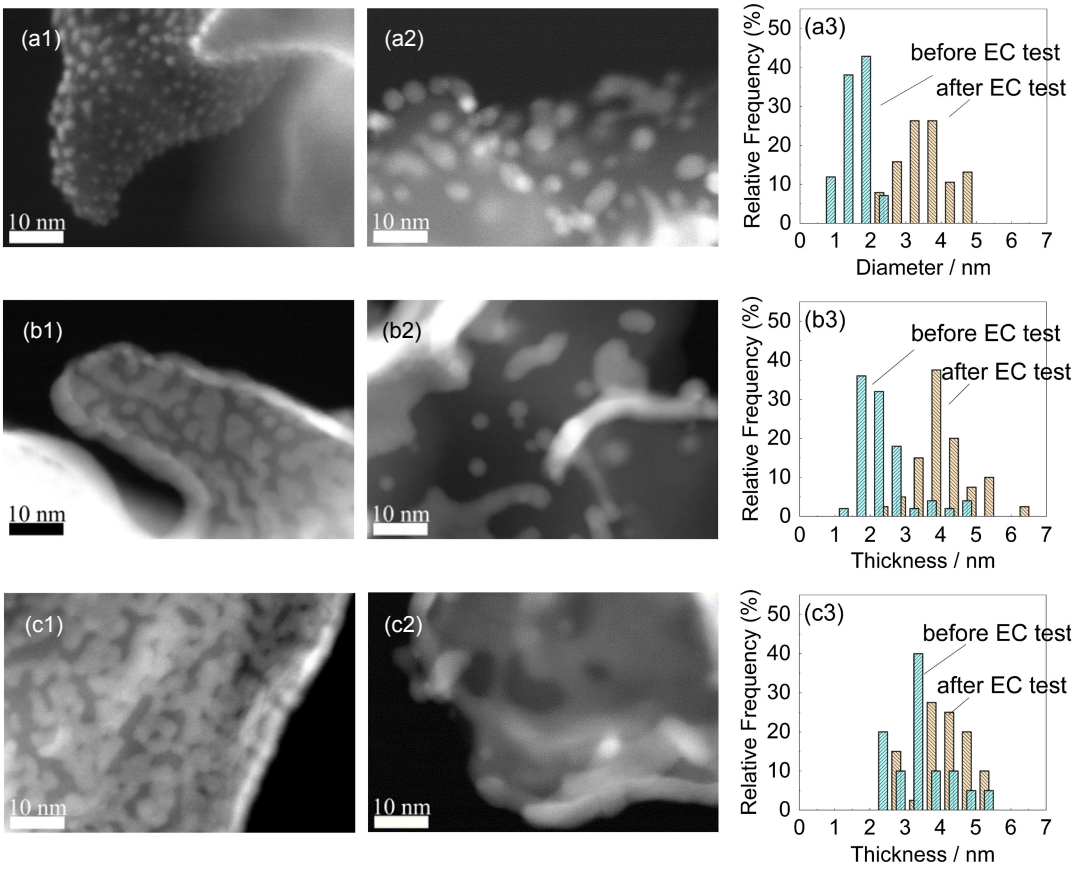

Figure 3. ADF-STEM images of Pt/Nb–Ti_4O_7. (a1) 2 wt%_Pt/Nb–Ti_4O_7 images before electrochemical test, (a2) 2 wt%_Pt/Nb–Ti_4O_7 images after electrochemical test, (b1) 5 wt%_Pt/Nb–Ti_4O_7 images before electrochemical test, (b2) 5 wt%_Pt/Nb–Ti_4O_7 images after electrochemical test, (c1) 10 wt%_Pt/Nb–Ti_4O_7 images before electrochemical test, (c2) 10 wt%_Pt/Nb–Ti_4O_7 images after electrochemical test, (a3, b3, c3) size distribution or thickness distribution of Pt deposits before/after electrochemical test.

titanium-oxide-based supports.[22,29,51–54] The details regarding the published supports are provided in Table S1.

In addition, comparing with other metal oxide supports,[29–54] the high conductivity of macroporous Nb–Ti_4O_7 was similar to those of Pt/Ta–$SnO_{2-\delta}$ and Pt/Nb–$SnO_{2-\delta}$,[53] for which it was reported that the conductivity increased significantly by Pt deposition and that the catalysts showed both high MA and SA are achieved. The low conductivity of supports can be significantly improved after Pt deposition (The Pt loadings of Pt/Ta–$SnO_{2-\delta}$ and Pt/Nb–$SnO_{2-\delta}$ were 15.8 wt% and 15.3 wt%, respectively) to ensure the performance of the catalysts. Moreover, conductivity in the range of 0.01–0.1 S cm^{-1} is expected for oxide-supported Pt catalysts. Therefore, the large surface area (46 m^2 g^{-1}) and the high conductivity (0.10 S cm^{-1}) of macroporous Nb–Ti_4O_7 are sufficient for its use as a support for PEFC cathodes.

3.2 Physical characterization of Pt/Nb–Ti_4O_7 catalysts

The annular dark field scanning transmission electron microscopy (ADF-STEM) images of the 2, 5, and 10 wt%_Pt/Nb–Ti_4O_7 catalysts prior to the ADTs are shown in Figs. 3(a1), 3(b1), and 3(c1), respectively. In each sample, Pt was deposited on the surface of a macroporous Nb–Ti_4O_7 support. Pt deposits were observed in most parts of the supports, whereas Pt nanoparticles were absent in some. Because Pt vapor was supplied from one direction in the APD, it was difficult to cover the surface of each support uniformly with Pt deposits. The presence of Pt deposits on most parts of the supports suggests that Pt vapor diffused around the particles. The shape, size, and density of Pt deposits depended on the number of shots in APD. When the Pt loading was 2 wt%, small nanoparticles were deposited on the surface of the support (Figs. 3(a1), S3a, and S3b), and they were disordered hemispheres in shape. Because of the high energy applied in APD, the deposited Pt nanoparticles possibly interacted strongly with the support to form the hemispherical shape,[55] a possible cause of the special morphology. The average size of the hemispheres, which corresponded to the length of the contact area between the Pt nanoparticles and the Nb–Ti_4O_7 support, was 1.4 nm (Fig. 3(a3)). A dense deposition of Pt nanoparticles is expected to result in their fusion. When the Pt loading was 5 wt%, the shape changed from hemispherical to island-like (Figs. 3(b1), S4a, and S4b), and tended to be film-like when the loading was further increased to 10 wt% (Figs. 3(c1), S5a, and S5b). For these cases, it is appropriate to use the average particle diameter to characterize the sizes of the island-like and film-like Pt deposits; therefore, the average thickness was used instead. The average thicknesses of the island-like 5 wt%_Pt/Nb–Ti_4O_7 and film-like 10 wt%_Pt/Nb–Ti_4O_7 catalysts were 2.4 and 3.3 nm, respectively (Figs. 3(b3) and 3(c3)). This suggests that the Pt prepared by APD extended horizontally without an increase in the thickness when the Pt loading increased from 5 to 10 wt%. Specifically, the flat area of the island-like Pt deposits increased, whereas the thickness did not, forming film-like Pt deposits. Therefore, the difference between the 5 and 10 wt%_Pt/Nb–Ti_4O_7 catalysts is their ratio of the edge-to-plane Pt deposits, with that of the former being larger than that of the latter owing to the connection of the island-like Pt deposits in 10 wt%_Pt/Nb–Ti_4O_7.

Figures 3(a2), 3(b2), and 3(c2) show the ADF-STEM images of the Pt/Nb–Ti_4O_7 catalysts after the ADTs. As shown in Figs. 3(a2), 3(a3), S3c, and S3d, the Pt nanoparticles of 2 wt%_Pt/Nb–Ti_4O_7 agglomerate, and the average particle size increases to 3.5 nm. In 5 wt%_Pt/Nb–Ti_4O_7, because the loading amount of Pt was half of

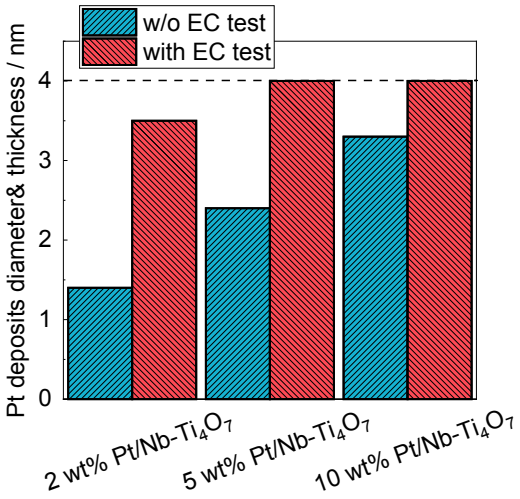

Figure 4. The Pt deposit diameter/thickness of Pt/Nb–Ti_4O_7 before and after the electrochemical test.

10 wt%_Pt/Nb–Ti_4O_7, some island-like Pt deposits connect to form chain bead-like Pt (Figs. 3(b2), S4c, and S4d). The thickness of the Pt deposits in 5 wt%_Pt/Nb–Ti_4O_7 increases slightly from 2.4 nm to 4.0 nm as an average, as shown in Fig. 3(b3). As shown in Figs. 3(c2), 3(c3), S5c, and S5d, because the Pt deposited in 10 wt%_Pt/Nb–Ti_4O_7 is film-like, the morphology and the thickness distribution change minimally during the ADTs. Figure 4 presents that despite the slight increase in the thickness, neither large particles nor thick films are formed, indicating that the Pt deposits prepared by APD do not thicken to above a range to 4 nm and that the island-like Pt deposits do not connect to form film-like Pt with a large flat plane. This morphological feature might be attributed to the strong interaction between Pt and Nb–Ti_4O_7 generated by APD. This unique degradation/morphological change may be caused by the surface energy of the crystal face, which leads to differences in the affinity of Pt.[56] Thus, the above characteristic grain growth of Pt/Nb–Ti_4O_7 could be caused by the high Pt affinity of Nb–Ti_4O_7.[57]

Figures 5a–5d depicts the changes in the CVs of the electrochemical properties of the catalysts during the ADTs, obtained at a scan rate of 50 mV s^{-1} from 0.05 to 1.2 V in 0.1 M $HClO_4$ at 60 °C. The initial parts of the CVs of the Pt/Nb–Ti_4O_7 and Pt/C catalysts are shown in Figs. S6a–S6d. Although all initial CVs of the catalysts presented typical Pt behavior, the hydrogen adsorption/desorption peaks of 2 wt%_Pt/Nb–Ti_4O_7 were ambiguous owing to the small amount of Pt. Its hydrogen adsorption peak was larger than the hydrogen desorption peak, which is known as a hydrogen spillover from Pt to the TiO_2 support.[58–60] Hydrogen spillover effect can occur when the TiO_2 support possesses rich and deficient oxygen vacancies[59] and Pt nanoparticles are covered with TiO_2.[60] In the present experiments, Pt was deposited by coaxial APD to form Pt/Nb–Ti_4O_7 in which the generated Pt ions are accelerated by a strong magnetic field induced in the coaxial arc plasma gun and are ejected toward the target substrate under vacuum. Miyazaki et al. employed STEM–electron energy loss spectroscopy analysis and determined that a GC substrate irradiated by Pt ions was damaged to depths of approximately 15–17 nm from the substrate surface.[61] In this study, the Pt nanoparticles partially penetrated the Nb–Ti_4O_7 support, resulting in the formation of hemisphere/flat-type Pt nanoparticles. Therefore, hydrogen spillover was observed in 2 wt%_Pt/Nb–Ti_4O_7. The CV of 10 wt%_Pt/Nb-Ti_4O_7 showed redox peaks at a range to 0.31 V, as presented in Figs. 5c and S6c. The morphology of the Pt deposits became film-like on increasing the Pt loading from 5 to 10 wt%, suggesting that the Pt (100) plane had extended. Pt (100) produced hydrogen adsorption-desorption peaks at a range to 0.3 V in 0.1 M $HClO_4$,[62] in the CV of 10 wt%_Pt/Nb–Ti_4O_7. Conversely, hydrogen adsorption-desorption peaks were observed at a range to 0.1 V in the CV of 5 wt%_Pt/Nb–Ti_4O_7, caused by Pt (110) in 0.1 M $HClO_4$.[62] Because the planar area of 5 wt%_Pt/Nb–Ti_4O_7 was smaller than that of the 10 wt% sample, the ratio of the edge-to-plane of 5 wt%_Pt/Nb–Ti_4O_7 was greater than that of 10 wt%. In other words, the ratio of Pt (110) to Pt (100) of 5 wt%_Pt/Nb–Ti_4O_7 was higher than that of 10 wt%. This difference affects the ORR activity, which is discussed subsequently. As shown in Figs. 5a–5d, the changes in the CV shapes of all Pt/Nb–Ti_4O_7 catalysts are comparatively lesser pronounced than that of Pt/C, suggesting that the ECSAs of the Pt/Nb–Ti_4O_7 catalysts are decreased to a small extent. Anomalous small anodic peaks are observed at 0.6–0.65 V vs. RHE in the CVs of 5 and 10 wt%_Pt/Nb–Ti_4O_7, as well as Pt/C, which are shown in Figs. 7a–7d. These peaks do not arise at room temperature. Sleightholme et al. established that these peaks increased with the increase in temperature and suggested that their origin is the formation of oxygenated species on the Pt surface.[63]

Figures 5e–5h show that the ECSAs of the catalysts decreases during the ADT. The ECSAs without ADT of the Pt/Nb–Ti_4O_7 catalysts with Pt loadings of 2, 5, and 10 wt% and Pt/C were calculated to be 45, 29, 28, and 91 $m^2 g^{-1}$, respectively. Although the ECSAs of 5 and 10 wt%_Pt/Nb–Ti_4O_7 were relatively small, that of 2 wt%_Pt/Nb–Ti_4O_7 was comparable to those of other Pt-supported titanium oxide-based catalysts. The small ECSAs of the 5 and 10 wt%_Pt/Nb–Ti_4O_7 catalysts were responsible for the formation of the island- and film-like Pt deposits (Figs. 3(b1), 3(c1), S4a, S4b, S5a, and S5b). The agglomeration of the Pt nanoparticles significantly decreased the ECSA of Pt/C until 3000 cycles. The ECSA of 2 wt%_Pt/Nb–Ti_4O_7 showed a slight decrease. However, the decreasing ratio of the 2 wt%_Pt/Nb–Ti_4O_7 ECSA rapidly decreased compared to that of Pt/C in the initial stage of the ADTs, as shown by the normalized catalyst ECSA changes in the inset of Fig. 5. Because the Pt particle size of 2 wt%_Pt/Nb–Ti_4O_7 was very small (average: 1.4 nm), it initially presented a propensity for agglomeration during the ADT and subsequently became stable. The 5 and 10 wt%_Pt/Nb–Ti_4O_7 catalysts demonstrated excellent ECSA stability, as shown in Figs. S7a–S7d. Overall, APD-deposited Pt slightly agglomerates during the ADTs, and different from the Pt/C catalyst, that Pt did not agglomerate into large-diameter spherical particles but had a tendency to connect and form thin film. This limited increase in the thickness reduced the decrease in the ECSA, particularly of the 5 and 10 wt%_Pt/Nb–Ti_4O_7 catalysts.

Figures 5i–5l present the changes in the platinum oxide reduction peak potential ($E_{Pt–O\ Reduction}$) among the electrochemical properties of the catalysts during the ADTs. $E_{Pt–O\ Reduction}$ reflects the adsorption energy for oxygenated species, which block the active sites for the ORR.[64,65] As shown in Figs. 5m–5p, before the ADTs, all the Pt/Nb–Ti_4O_7 catalysts possess higher $E_{Pt–O\ Reduction}$ than Pt/C. The positive shift in $E_{Pt–O\ Reduction}$ suggests a decrease in the adsorption energy for the oxygenated species. The relationship between this peak shift and the SA will be discussed subsequently. As shown in Figs. 5i–5l and 5m–5p, the $E_{Pt–O\ Reduction}$ of the 2 wt%_Pt/Nb–Ti_4O_7 catalyst gradually shifts to a higher potential as the particle size increases.[64] However, the extent of the potential shift is smaller than that of Pt/C. The 5 and 10 wt%_Pt/Nb–Ti_4O_7 catalysts demonstrated excellent ECSA stability, as shown in Figs. 5f and 5g. The changes in their CVs are minimal, indicating that the $E_{Pt–O\ Reduction}$ similarly do not shift remarkably.

Figure 6 shows the decrease in the ECSAs with the $E_{Pt–O\ Reduction}$ increase of each catalyst during the ADTs. The plots with the green right-hand triangle and blue upper triangle are the initial and post-ADT results, respectively. A similar relationship as found here was observed in a previous study.[64] From the viewpoint of the Pt particle

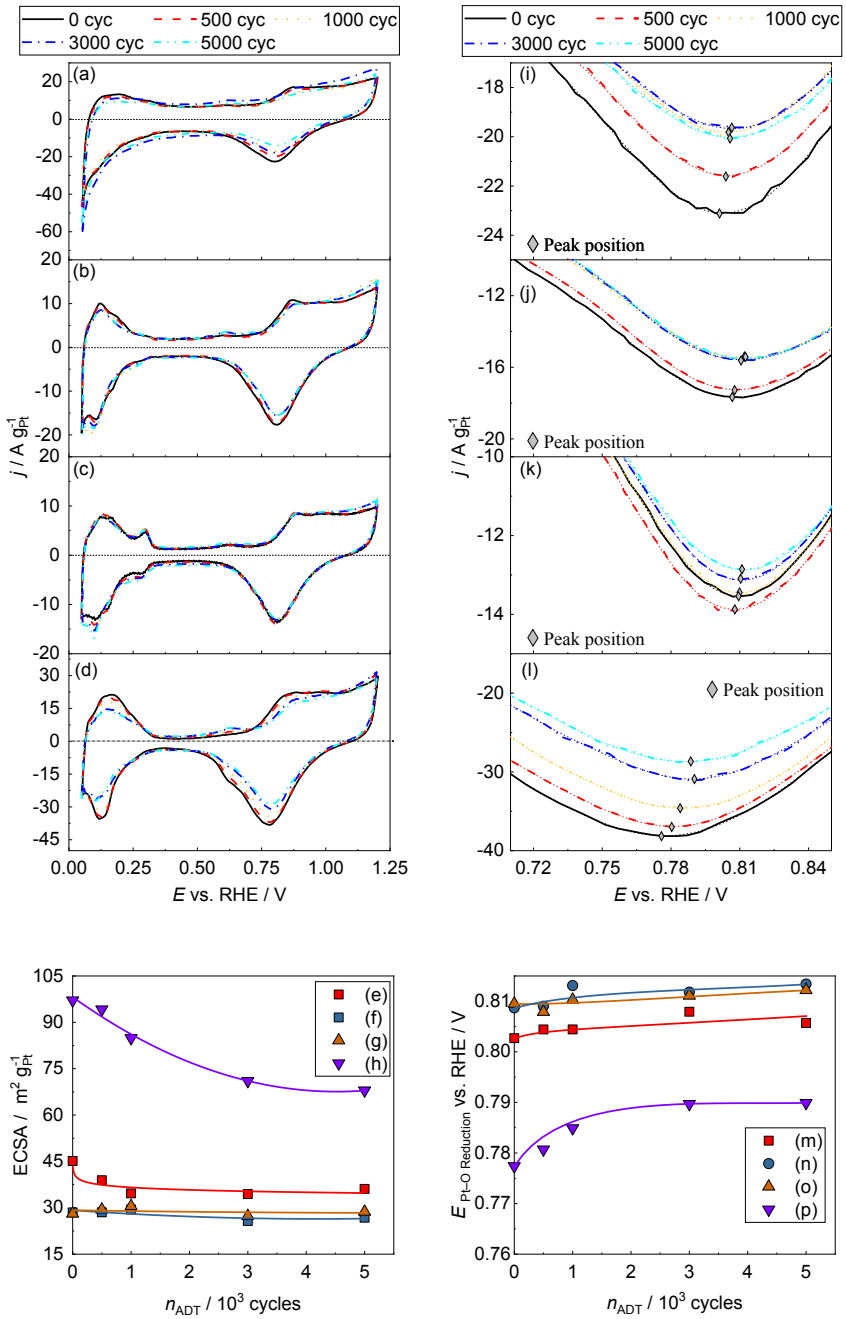

Figure 5. CVs of (a) 2 wt%_Pt/Nb–Ti_4O_7, (b) 5 wt%_Pt/Nb–Ti_4O_7, (c) 10 wt%_Pt/Nb–Ti_4O_7, and (d) Pt/C during ADT; decrease in ECSAs (e) 2 wt%_Pt/Nb–Ti_4O_7, (f) 5 wt%_Pt/Nb–Ti_4O_7, (g) 10 wt%_Pt/Nb–Ti_4O_7, and (h) Pt/C as a function of ADT cycles (n_{ADT}); Pt–O reduction peak shifts of (i) 2 wt%_Pt/Nb–Ti_4O_7, (j) 5 wt%_Pt/Nb–Ti_4O_7, (k) 10 wt%_Pt/Nb–Ti_4O_7, and (l) Pt/C during ADTs and the shifts in Pt–O reduction peaks of (m) 2 wt%_Pt/Nb–Ti_4O_7, (n) 5 wt%_Pt/Nb–Ti_4O_7, (o) 10 wt%_Pt/Nb–Ti_4O_7, and (p) Pt/C as a function of ADT cycles (n_{ADT}).

size, a larger ECSA implies a small particle size of Pt and strong adsorption on oxygen to form stronger Pt–O bonds.[6] The stronger Pt–O bonds, in turn, cause a small shift in the $E_{Pt–O\ Reduction}$, resulting in a large ECSA and low $E_{Pt–O\ Reduction}$ of Pt/C. For 2 wt%_Pt/Nb–Ti_4O_7 prior to the ADTs, although the average Pt particle size was small (1.4 nm), the initial ECSA was approximately half that of Pt/C, and a relatively high $E_{Pt–O\ Reduction}$ was obtained. This was a consequence of the hemispheric morphology of the deposited Pt nanoparticles in 2 wt%_Pt/Nb–Ti_4O_7, different from Pt/C, because of the high discharge energy in APD and the high affinity. The hemispheric morphology, in turn, decreased the ECSA because the contact area between the Pt nanoparticles and support was not in contact with the electrolyte. The relatively high $E_{Pt–O\ Reduction}$ of the 2 wt%_Pt/Nb–Ti_4O_7 catalyst resulted from the interaction between the Pt nanoparticles and the Nb–Ti_4O_7 support. Because the Pt in 5 and 10 wt%_Pt/Nb–Ti_4O_7 was deposited in the island-like and film-like morphologies, respectively, their ECSAs were comparable. In both 5 and 10 wt%_Pt/Nb–Ti_4O_7, the surface of the contact interface between the Pt deposits and the electrolyte was probably predominantly Pt (100), resulting in their comparable $E_{Pt–O\ Reduction}$ values. As the ADTs progressed, the ECSA and $E_{Pt–O\ Reduction}$ of 2 wt%_Pt/Nb–Ti_4O_7 and Pt/C changed simultaneously linearly. These tendencies can be understood as the properties of the Pt nanoparticles.[63] In contrast, the plots of 5 and 10 wt%_Pt/Nb–Ti_4O_7 remained the same. This difference in behavior was a consequence of the differences in the morphology of the deposited Pt.

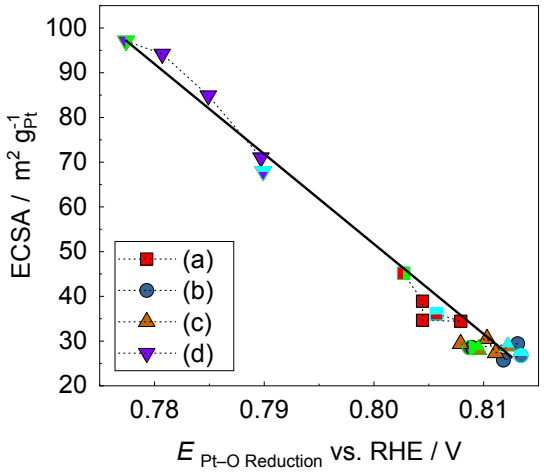

Figure 6. Decrease in ECSAs with Pt–O reduction peaks shift to high potential side during ADTs (a) 2 wt%_Pt/Nb–Ti_4O_7, (b) 5 wt%_Pt/Nb–Ti_4O_7, (c) 10 wt%_Pt/Nb–Ti_4O_7, and (d) Pt/C.

The Tafel plots of the MAs of catalysts during the ADTs are shown in Figs. 7a–7d, Figs. S8a–S8d are the initial MAs. The changes in the MA and SA at 0.9 V vs. RHE with the cycle number of the ADT are shown in Figs. 7e–7h and 7i–7l, respectively. The order of the initial MAs for the ORR at 0.9 V is 2 wt% (117 A g^{-1}) > 5 wt% (72 A g^{-1}) > Pt/C (47 A g^{-1}) > 10 wt%_Pt/Nb–Ti_4O_7 (36 A g^{-1}), in Figs. S8a–S8d. The MAs of the 2 and 5 wt%_Pt/Nb–Ti_4O_7 are sufficiently high, although the ECSAs are small, suggesting that their SAs are substantially high. Herein, before the ADTs, the Pt/C SA for the ORR is low because Pt nanoparticles with a small particle size strongly adsorb oxygenated species, as shown in Fig. S9, which also results in low $E_{Pt–O\ Reduction}$. The SA of 2 wt%_Pt/Nb–Ti_4O_7 was high, although its Pt particle size was small, because the interaction between the Pt nanoparticles and Nb–Ti_4O_7 enhanced the ORR activity via a mechanism similar to that discussed in previous studies.[18,24–29,32–35,37] In contrast, the SA of 10 wt%_Pt/Nb–Ti_4O_7 was approximately half that of the 2 wt% catalyst, because of the large Pt (100) plane area of the former on which the SA for the ORR is relatively low.[62] Although the $E_{Pt–O\ Reduction}$ of 10 wt%_Pt/Nb–Ti_4O_7 was higher than that of the 2 wt% analogue, the smaller SA of the former was caused by its morphology, which differs from that of 2 wt%_Pt/Nb–Ti_4O_7 (film-like vs. nanoparticles, respectively). The SA of the 5 wt%_Pt/Nb–Ti_4O_7 catalyst was comparable to that of the 2 wt% analogue, whereas its $E_{Pt–O\ Reduction}$ was similar to that of 10 wt%_Pt/Nb–Ti_4O_7. Regarding the CV shapes, the ratio of Pt (110) to Pt (100) in 5 wt%_Pt/Nb–Ti_4O_7 was greater than those of the 10 wt% sample. The ORR SA in 0.1 M $HClO_4$ increased in the order Pt (110) > Pt (111) > Pt (100).[62] The increase in the Pt (110) of 5 wt%_Pt/Nb–Ti_4O_7 causes an increase in the SA, as shown in Fig. 8.

As described above, the difference in the agglomeration among the Pt/Nb–Ti_4O_7 catalysts may be caused by the differences in the affinity. Sheng et al. reported a surface energy order of {111} < {100} < {110} facet.[56,66] Because the ratio of Pt (110) to Pt (100) in 5 wt%_Nb–Ti_4O_7 is greater than that in 10 wt%_Nb–Ti_4O_7 and the latter had a large Pt (100) plane area, the surface energy followed the order: 5 wt% > 10 wt% > 2 wt%_Nb–Ti_4O_7. Moreover, a high surface energy causes substrates to be held by bonds, and high-surface

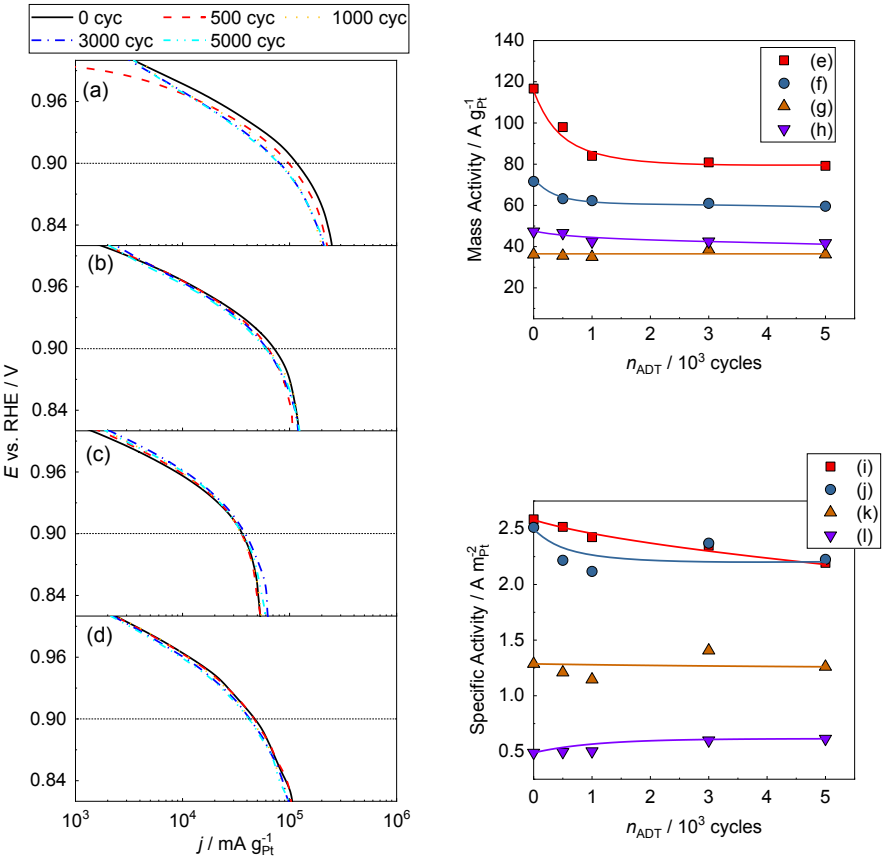

Figure 7. Tafel plots of MA of Pt/Nb–Ti_4O_7 and Pt/C during ADTs, (a) 2 wt%_Pt/Nb–Ti_4O_7, (b) 5 wt%_Pt/Nb–Ti_4O_7, (c) 10 wt%_Pt/Nb–Ti_4O_7, and (d) Pt/C; the decrease of MA at 0.9 V vs. RHE as a function of ADT cycles (n_{ADT}): (e) 2 wt%_Pt/Nb–Ti_4O_7, (f) 5 wt%_Pt/Nb–Ti_4O_7, (g) 10 wt%_Pt/Nb–Ti_4O_7, and (h) Pt/C; and decrease in SA at 0.9 V vs. RHE as a function of ADT cycles (n_{ADT}): (i) 2 wt%_Pt/Nb–Ti_4O_7, (j) 5 wt%_Pt/Nb–Ti_4O_7, (k) 10 wt%_Pt/Nb–Ti_4O_7, and (l) Pt/C.

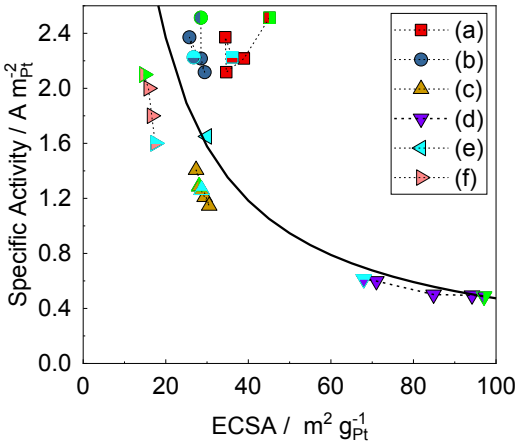

Figure 8. Effects of ADT showing specific activity increase with ECSA decreasing at 0.9 V of (a) 2 wt%_Pt/Nb–Ti_4O_7, (b) 5 wt%_Pt/Nb–Ti_4O_7, (c) 10 wt%_Pt/Nb–Ti_4O_7, (d) Pt/C in this work and in Ref. 33, (e) Pt/oxide catalyst in Ref. 33, and (f) Pt/oxide catalyst in Ref. 25. The "green right-hand half" triangles are the initial results, and the "blue upper half" triangles are after 5000 cycles of ADT. The curve was drawn based on the data of Pt/C catalysts in this study and in Ref. 33.

energy substrates are easily wetted.[67] The low-energy 2 wt%_Nb–Ti_4O_7 was easier to agglomerate during the ADT than the other Pt/Nb–Ti_4O_7 catalysts, and although the high-energy 5 wt%_Nb–Ti_4O_7 did not have a film-like morphology that is relatively difficult to agglomerate, its ECSA decline rate and morphological changes were very limited. In addition, surface energy is positively correlated with the catalytic activity,[66,68] and it also could explain the high SA of 5 wt%_Pt/Nb–Ti_4O_7.

Figure 7e during the ADTs, the MA of the 2 wt%_Pt/Nb–Ti_4O_7 catalyst decreases significantly in the first 1000 cycles, following which it remains virtually constant. As shown in Fig. 7i, although the decrease in the SA of 2 wt%_Pt/Nb–Ti_4O_7 is not substantial, there is a significant decrease in its MA, which results from the decrease in both the ECSA and SA. In contrast, despite the large decrease in the ECSA of Pt/C (Fig. 5h), its MA decreases slightly with each ADT cycle. This is caused by the SA of Pt/C increasing with the Pt particle size increased due to agglomeration. In the case of the carbon support, the agglomeration of Pt nanoparticles decreases in the ECSA and shifts the $E_{Pt–O\ Reduction}$ to a higher potential, increasing the SA, as shown in Figs. 6 and 7l. For 2 wt%_Pt/Nb–Ti_4O_7, the tendencies of the ECSA and $E_{Pt–O\ Reduction}$ with the ADT progress are similar to those of Pt/C, as shown in Fig. 6. However, the change in the SA of 2 wt%_Pt/Nb–Ti_4O_7 with respect to the number of ADT cycles is dissimilar to that of Pt/C, is the difference between the carbon- and oxide-based supports. The SA of the 2 wt%_Pt/Nb–Ti_4O_7 catalyst is high because of the strong interaction between the Pt nanoparticles and the Nb–Ti_4O_7 support when the Pt particle size is sufficiently small, presumably less than 2 nm. As the Pt particle size increases, the interaction weakens, resulting in a gradual decrease in the SA. After 1000 ADT cycles, both the ECSA and SA are virtually constant, and the SA is comparable to that of the 5 wt% sample. In comparison with Pt/C and 2 wt%_Pt/Nb–Ti_4O_7, 5 and 10 wt%_Pt/Nb–Ti_4O_7 are considerably more stable, although some fluctuations were observed in the first 1000 cycles. Because the ECSAs of 5 and 10 wt%_Pt/Nb–Ti_4O_7 were similar, their MAs were governed by the SAs. The slight decrease in the SA of 5 wt%_Pt/Nb–Ti_4O_7 resulted in a small decrease in the MA. In contrast, in the case of 10 wt%_Pt/Nb–Ti_4O_7, the deterioration of both the SA and MA during the ADT was negligible.

Additionally, Nie et al. reported the spatial heterogeneity of electron transfer on a metallic nanoplate prism.[69] They suggested that the dipole moment and polarizability of intermediate species can be modified when changing interfacial electric field according to microkinetic models so that at its corner and edge dominate the local enhancement in the electron transfer. In the experiments, 5 wt%_Pt/Nb–Ti_4O_7 deposited by APD presented an island-like shape Pt (Figs. 3(b1), S4a, and S4b). Although the vertical projected area of its Pt deposits was larger than that of 2 wt%_Pt/Nb–Ti_4O_7, the former had more remarkable edges. Furthermore, after the ADTs, some island-like deposited Pt of 5 wt%_Pt/Nb–Ti_4O_7 connected to form chain-like Pt (Figs. 3(b2), S4c, and S4d). Thus, the Pt aggregation in the ADTs leads to the formation of a relatively higher proportion of edges and corners, which contribute to more ORR current than on the basal site. This also explains that although the MA and ECSA were not high as those of 2 wt%_Pt/Nb–Ti_4O_7, 5 wt%_Pt/Nb–Ti_4O_7 showed a similar SA, which was stable during the ADTs.

Figure 8 shows the effect of the ADTs on the relationship between the ECSA and SA of the catalysts. For comparison, previous results are also plotted. The plots in green right-hand triangles and blue upper triangles present the initial and post-ADT results, respectively. The contour line of the MA of the initial Pt/C (47 A g^{-1} @ 0.9 V) is shown.[25,33] Herein, the curve was drawn according to initial SA × ECSA = 47, which could be fitted with the data of Pt/C catalysts. The plots located on the right-hand side of the contour line indicated a larger MA of the initial Pt/C, revealing that the 2 and 5 wt%_Pt/Nb–Ti_4O_7 catalysts possessed larger MAs than Pt/C in the initial stage. The tracks of each catalyst reflect its electrochemical stability. The tracks of Pt/C gradually moved away from the contour line, indicating that the MA of Pt/C gradually decreased from its initial value. Because the tracks of 10 wt%_Pt/Nb–Ti_4O_7 are close to the contour line, its MA remains unchanged, although it is consistently lower than that of Pt/C. The initial MAs of 2 and 5 wt%_Pt/Nb–Ti_4O_7 are higher than those of Pt/C. The tracks of 2 and 5 wt%_Pt/Nb–Ti_4O_7 are consistently on the right-hand side of the contour line until 5000 cycles, demonstrating that the MAs of these catalysts remained higher than the initial MA of Pt/C, even after the ADT. After 5000 ADT cycles, although the SAs of 2 and 5 wt%_Pt/Nb–Ti_4O_7 were comparable, the difference in their ECSAs remained, thereby resulting in the difference in their MAs. Table 1 summarizes the initial electrochemical properties and durability of the catalysts in comparison with previous results.

To investigate the differences in the electronic states of the Pt deposits in the Pt/Nb–Ti_4O_7 and Pt/C catalysts before and after the electrochemical tests, Pt 4f XPS spectra were recorded, which are shown in Figs. 9a–9h. The center positions of the peaks of 2, 5, and 10 wt%_Pt/Nb–Ti_4O_7 were shifted to lower energy side than that of Pt/C. Therefore, the peak separation was performed to find the specific features of the electronic states of Pt in the Pt/Nb–Ti_4O_7. The metallic Pt was separated as an asymmetric line shape, whereas the Pt oxides were distinguished by a symmetric line shape. Before the electrochemical test, two peaks were observed in the Pt 4f region, and each peak could be deconvoluted into several peaks corresponding to Pt species in distinct electronic states (Pt^0, Pt^{2+}, Pt^{4+}). The valence states ratios are shown in Figs. 10a and 10b.

Figure 10a shows the percentages of Pt^0, Pt^{2+}, and Pt^{4+}, deduced from the XPS spectra before the electrochemical test. The ratios of Pt^0 in 5 and 10 wt%_Pt/Nb–Ti_4O_7 were higher than those in 2 wt%_Pt/Nb–Ti_4O_7 and Pt/C. This tendency can be explained by the electron donation from the Nb–Ti_4O_7 support to the deposited Pt. In contrast, a small Pt particle size (<2 nm) leads to higher adsorption energy of the oxygenated species;[6] therefore, the Pt nanoparticles of 2 wt%_Pt/Nb–Ti_4O_7 were partially oxidized in air owing to their small particle sizes (average: 1.4 nm), resulting in a smaller ratio of metallic Pt compared to those in 5 and 10 wt%_Pt/

Table 1. Comparison with other Pt/metal oxides catalysts.

	Support	Pt wt%	Before ADT			After ADT			θ / °C	ADT
			ECSA $m^2\,g^{-1}$	MA $A\,g^{-1}$ @ 0.9 V vs. RHE	SA $A\,m^{-2}$ @ 0.9 V vs. RHE	ECSA $m^2\,g^{-1}$	MA $A\,g^{-1}$ @ 0.9 V vs. RHE	SA $A\,m^{-2}$ @ 0.9 V vs. RHE		
This study	Nb–Ti_4O_7	2	45	117	2.59	36	79	2.19	60	1.0–1.5 V 500 mV s^{-1} (5k cyc)
		5	29	72	2.51	27	60	2.23		
		10	28	36	1.29	29	36	1.26		
	Ketjen black	46.43	97	47	0.49	68	41	0.61		
Ref. 25	Nb–TiO_2 Fibers	40 ALD cycles	14.74		2.1			1.6		0.6–1.0 V 100 mV s^{-1} (30k cyc)
Ref. 26	TiO_2	20	14.17	1.83	0.129		1.02		25	0.6–1.0 V 25 mV s^{-1} (5k cyc)
	TiO_2–HT *HT = heat treatment*		10.22	1.01	0.099		3.69			
	TiO_2–HFT *HFT = heat treatment and hydrofluoric acid treatment*		15.19	4.23	0.276					
	TiO_2–FT *FT = directly hydrofluoric acid treatment*		15.67	2.07	0.132					
	$TiNbO_2$			13	0.65					
	$TiNbO_2$–HFT			24	1.3					
Ref. 29	TiO_x	17.93		1.37	0.49		0.47		25	0.6–1.0 V 25 mV s^{-1} (5k cyc)
		18.03		0.97	0.35					
Ref. 33	Nb–TiO_2	20	42.5	70	1.65				25	
Ref. 51	Nb–doped TiO_2	20	30	5.3	0.85	26.4	3.6		20	1.2–0.2 V 100 mV s^{-1} (1k cyc)
Ref. 54	Ti_4O_7	39.28	39.28		9.73					

Nb–Ti_4O_7. Overall, Pt deposits with a large ratio of metallic Pt on Nb–Ti_4O_7 were successfully fabricated by APD.

Figure 10b shows the composition of the valence states of Pt in the catalysts after the electrochemical test, calculated using the peak separation of the Pt 4f XPS, as shown in Figs. 9a–9h. Compare with the valence states ratio in Fig. 10a, the Pt valence state composition in all of the Pt/Nb–Ti_4O_7 catalysts reaches a similar level, presenting a large ratio of Pt^0 and a few Pt oxides after the ADT. Owing to the size of 2 wt%_Pt/Nb–Ti_4O_7 increased, and the shape transferred to the island-like, the adsorption energy would be decreased and hard to be oxidized. The Pt^0 ratios of the Pt/Nb–Ti_4O_7 catalysts are larger than those of Pt/C, suggesting that the interaction between Pt and Nb–Ti_4O_7 remains after the ADT.

Although smaller Pt nanoparticles are favorable for achieving a large ECSA from the viewpoint of the MA, they are unstable even when they strongly interact with the Nb–Ti_4O_7 support. A Pt deposit with a thickness of approximately 4 nm is advantageous from the perspective of stability because such Pt deposits prepared by APD are stable. Pt nanoparticles with a diameter of approximately 4 nm or island-like Pt deposits with a thickness of approximately 4 nm and abundant edges, such as Pt (110), are beneficial for both the MA and stability of Pt/Nb–Ti_4O_7 catalysts prepared by APD.

4. Conclusions

Highly active and durable Pt catalysts for the ORR are required to enable the widespread use of PEFCs. As model Pt catalysts, 2, 5, and 10 wt% Pt were deposited onto synthesized macroporous Nb–Ti_4O_7 support by APD method. The morphologies with 2, 5, and 10 wt% Pt loadings were fine hemispherical with particle size ca. 1.4 nm, island-like with ca. 2.4 nm, and film-like with 3.3 nm thickness, respectively. After 5000 cycles of the ADTs, large spherical Pt particle agglomeration in any Pt/Nb–Ti_4O_7 catalyst; however, Pt was formed as island-like with ca. 3.5 nm thickness, chain bead-like with ca. 4 nm of thickness, and film-like with ca. 4 nm thickness, respectively. The ECSAs of 2, 5, and 10 wt% Pt/Nb–Ti_4O_7 were 36 $m^2\,g^{-1}$ with 20% decrease ratio, 27 $m^2\,g^{-1}$ with 6 % decrease ratio, and 29 $m^2\,g^{-1}$ with no decrease respectively. All were more durable than Pt/C, which possessed an ECSA of 68 $m^2\,g^{-1}$ with 30 % of decrease ratio after the ADTs. The MA at 0.9 V vs. RHE was declined 32 %, 17 %, and no decrease respectively after the ADT, and 5 wt% and 10 wt% Pt/Nb–Ti_4O_7 presented good durability compared with Pt/C, which decreased 12 % after ADT. In addition, the MAs after the ADTs were comparable to that of Pt/C (42 A g_{Pt}^{-1}), reaching 79, 60, and 36 A g_{Pt}^{-1} with 2, 5, and 10 wt% Pt loadings, respectively. Pt/Nb–Ti_4O_7 contained a relatively higher proportion of metal Pt both before and after the electrochemical test than Pt/C. The ADT results exhibited that the Pt deposits prepared via APD became stable at a thickness of approximately 4 nm, and this slight agglomeration, which might be caused by the different affinities of the Pt deposits crystal faces on Nb–Ti_4O_7 by APD, led to their high durability in the ADTs.

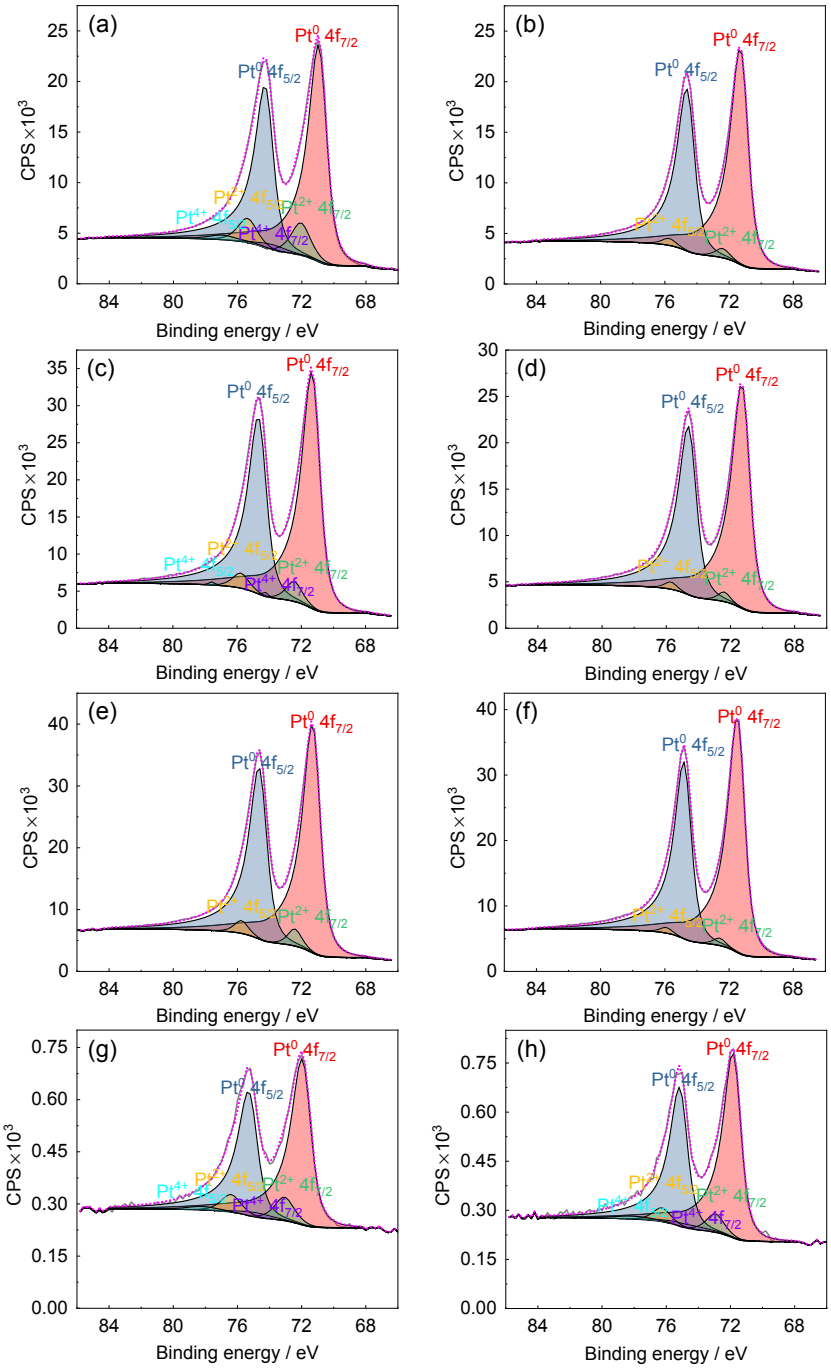

Figure 9. Pt 4f XPS spectra of Pt/Nb–Ti_4O_7 before electrochemical test: (a) 2 wt%_Pt/Nb–Ti_4O_7, (b) 5 wt%_Pt/Nb–Ti_4O_7, (c) 10 wt%_Pt/Nb–Ti_4O_7, and (d) Pt/C; Pt 4f XPS spectra of Pt/Nb–Ti_4O_7 after electrochemical test: (e) 2 wt%_Pt/Nb–Ti_4O_7, (f) 5 wt%_Pt/Nb–Ti_4O_7, (g) 10 wt%_Pt/Nb–Ti_4O_7, and (h) Pt/C.

The high affinity between Pt and Nb–Ti_4O_7 causes a limited increase in the thickness. The different affinities and the high energy of APD lead to distinct morphologies of the Pt deposits on Nb–Ti_4O_7, and the different affinities of the Pt deposits crystal faces on Nb–Ti_4O_7 by APD cause differences in the durability and activity of Pt/Nb–Ti_4O_7. Additionally, the electron transfer of the different morphologies and the SMSI between Pt and Nb–Ti_4O_7 might be beneficial for the improvement in the activity and the durability. Furthermore, it is suggested that among Pt/oxide catalysts, island-shape Pt deposits with a limited thickness, possessing high density and uniform deposition on the surface of the support, would contribute to both durability and activity.

Acknowledgment

This research was supported by Strategic International Research Cooperative Program, Japan Science and Technology Agency (JST). This work was also supported in part by JSPS KAKENHI Grant No. 17K06803. STEM and XPS were performed by CLEARIZE Co., Ltd. We would like to thank Mr. Y. Ohtsu, Mr. A. Yokota, and Mr. S. Ohtsu of CLEARIZE Co., Ltd.

CRediT Authorship Contribution Statement

Yongbing Ma: Conceptualization (Lead), Writing – original draft (Lead)
Hirokata Kajima: Methodology (Equal)

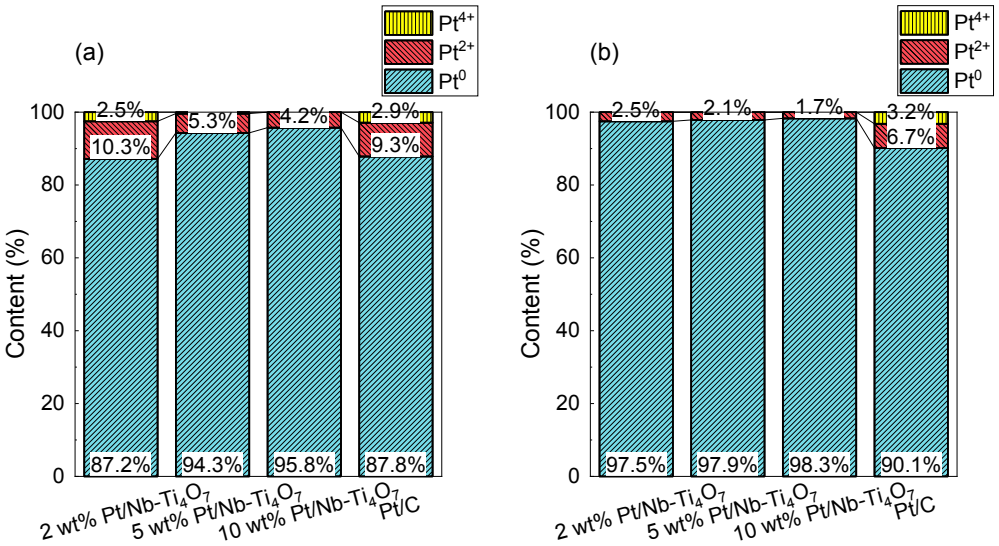

Figure 10. (a) Percentages of different valence calculated by XPS before electrochemical test; (b) percentages of different valence calculated by XPS after electrochemical test.

Yuta Shimasaki: Methodology (Equal)
Takaaki Nagai: Data curation (Supporting), Formal analysis (Supporting)
Teko W. Napporn: Formal analysis (Equal)
Hiroaki Wada: Writing – review & editing (Supporting)
Kazuyuki Kuroda: Writing – review & editing (Supporting)
Yoshiyuki Kuroda: Supervision (Lead)
Akimitsu Ishihara: Funding acquisition (Lead), Supervision (Lead)
Shigenori Mitsushima: Funding acquisition (Lead), Supervision (Lead)

Data Availability Statement

The data that support the findings of this study are openly available under the terms of the designated Creative Commons License in J-STAGE Data listed in D1 of References.

Conflict of Interest

The authors declare no conflict of interest in the manuscript.

Funding

Japan Society for the Promotion of Science: 17K06803
Japan Science and Technology Agency

References

D1. Y. Ma, H. Kajima, Y. Shimasaki, T. Nagai, T. W. Napporn, H. Wada, K. Kuroda, Y. Kuroda, A. Ishihara, and S. Mitsushima, *J-STAGE Data*, https://doi.org/10.50892/data.electrochemistry.19586680, (2022).
1. A. Esmaeilifar, S. Rowshanzamir, M. Eikani, and E. Ghazanfari, *Energy*, **35**, 3941 (2010).
2. S. Sun, G. Zhang, D. Geng, Y. Chen, R. Li, M. Cai, and X. Sun, *Angew. Chem., Int. Ed.*, **123**, 442 (2011).
3. H. T. Chung, H. Zhang, J. Park, D. A. Cullen, K. L. More, D. J. Myers, E. E. Alp, and P. Zelenay, in *ECS Meeting Abstracts*, p. 1680 (2020).
4. N. Kameda, M. Nakamura, and N. Hoshi, *Electrochemistry*, **89**, 1 (2021).
5. L. Roen, C. Paik, and T. Jarvi, *Electrochem. Solid-State Lett.*, **7**, A19 (2004).
6. M. Shao, A. Peles, and K. Shoemaker, *Nano Lett.*, **11**, 3714 (2011).
7. F. Hasché, M. Oezaslan, and P. Strasser, *ECS Trans.*, **41(1)**, 1079 (2011).
8. L. Dubau, T. Asset, R. l. Chattot, C. l. Bonnaud, V. Vanpeene, J. Nelayah, and F. D. R. Maillard, *ACS Catal.*, **5**, 5333 (2015).
9. C. Cui, L. Gan, H.-H. Li, S.-H. Yu, M. Heggen, and P. Strasser, *Nano Lett.*, **12**, 5885 (2012).
10. Y. Kang, J. Snyder, M. Chi, D. Li, K. L. More, N. M. Markovic, and V. R. Stamenkovic, *Nano Lett.*, **14**, 6361 (2014).
11. L. Chong, J. Wen, J. Kubal, F. G. Sen, J. Zou, J. Greeley, M. Chan, H. Barkholtz, W. Ding, and D.-J. Liu, *Science*, **362**, 1276 (2018).
12. Y. Shao, G. Yin, and Y. Gao, *J. Power Sources*, **171**, 558 (2007).
13. G. Wang, K. Bhattacharyya, J. Parrondo, and V. Ramani, *Chem. Eng. Sci.*, **154**, 81 (2016).
14. E. C. Barbosa, L. S. Parreira, I. C. de Freitas, L. R. Aveiro, D. C. de Oliveira, M. C. dos Santos, and P. H. Camargo, *ACS Appl. Energy Mater.*, **2**, 5759 (2019).
15. Y. Kuroda, H. Igarashi, T. Nagai, T. W. Napporn, K. Matsuzawa, S. Mitsushima, K.-I. Ota, and A. Ishihara, *Electrocatalysis*, **10**, 459 (2019).
16. S. Andersson, B. Collén, U. Kuylenstierna, and A. Magnéli, *Acta Chem. Scand.*, **11**, 1641 (1957).
17. J. Smith, F. Walsh, and R. Clarke, *J. Appl. Electrochem.*, **28**, 1021 (1998).
18. T. Ioroi, H. Senoh, S.-I. Yamazaki, Z. Siroma, N. Fujiwara, and K. Yasuda, *J. Electrochem. Soc.*, **155**, B321 (2008).
19. C. Yao, F. Li, X. Li, and D. Xia, *J. Mater. Chem.*, **22**, 16560 (2012).
20. A. Gusev, E. Avvakumov, and O. Vinokurova, *Sci. Sinter.*, **35**, 141 (2003).
21. D. Kundu, R. Black, E. J. Berg, and L. F. Nazar, *Energy Environ. Sci.*, **8**, 1292 (2015).
22. Y. Ma, T. Nagai, Y. Inoue, K. Ikegami, Y. Kuroda, K. Matsuzawa, T. W. Napporn, Y. Liu, S. Mitsushima, and A. Ishihara, *Mater. Des.*, **203**, 109623 (2021).
23. M. Iwami, D. Horiguchi, Z. Noda, A. Hayashi, and K. Sasaki, *ECS Trans.*, **69(17)**, 603 (2015).
24. C. He, S. Sankarasubramanian, I. Matanovic, P. Atanassov, and V. Ramani, *ChemSusChem*, **12**, 3468 (2019).
25. Q. Du, J. Wu, and H. Yang, *ACS Catal.*, **4**, 144 (2014).
26. B.-J. Hsieh, M.-C. Tsai, C.-J. Pan, W.-N. Su, J. Rick, H.-L. Chou, J.-F. Lee, and B.-J. Hwang, *Electrochim. Acta*, **224**, 452 (2017).
27. Q. Jia, S. Ghoshal, J. Li, W. Liang, G. Meng, H. Che, S. Zhang, Z.-F. Ma, and S. Mukerjee, *J. Am. Chem. Soc.*, **139**, 7893 (2017).
28. M.-C. Tsai, T.-T. Nguyen, N. G. Akalework, C.-J. Pan, J. Rick, Y.-F. Liao, W.-N. Su, and B.-J. Hwang, *ACS Catal.*, **6**, 6551 (2016).
29. A. D. Duma, Y. C. Wu, W. N. Su, C. J. Pan, M. C. Tsai, H. M. Chen, J. F. Lee, H. S. Sheu, V. T. T. Ho, and B. J. Hwang, *ChemCatChem*, **10**, 1155 (2018).
30. V. T. T. Ho, C.-J. Pan, J. Rick, W.-N. Su, and B.-J. Hwang, *J. Am. Chem. Soc.*, **133**, 11716 (2011).
31. T. B. Do, M. Cai, M. S. Ruthkosky, and T. E. Moylan, *Electrochim. Acta*, **55**, 8013 (2010).
32. S. Sun, G. Zhang, X. Sun, M. Cai, and M. Ruthkosky, *J. Nanotechnol.*, **2012**, 389505 (2012).
33. N. R. Elezović, B. M. Babić, L. Gajić-Krstajić, V. Radmilović, N. Krstajić, and L. Vračar, *J. Power Sources*, **195**, 3961 (2010).
34. B.-J. Hsieh, M.-C. Tsai, C.-J. Pan, W.-N. Su, J. Rick, J.-F. Lee, Y.-W. Yang, and B.-J. Hwang, *NPG Asia Mater.*, **9**, e403 (2017).
35. S. H. Kim, C.-H. Jung, N. Sahu, D. Park, J. Y. Yun, H. Ha, and J. Y. Park, *Appl. Catal., A*, **454**, 53 (2013).
36. Y. Agawa, M. Kunimatsu, T. Ito, Y. Kuwahara, and H. Yamashita, *ECS Electrochem. Lett.*, **4**, F57 (2015).
37. N. Todoroki, T. Kato, T. Hayashi, S. Takahashi, and T. Wadayama, *ACS Catal.*, **5**, 2209 (2015).
38. C. Xu, J. Yang, E. Liu, Q. Jia, G. M. Veith, G. Nair, S. DiPietro, K. Sun, J. Chen, and P. Pietrasz, *J. Power Sources*, **451**, 227709 (2020).
39. M. Kitahara, Y. Shimasaki, T. Matsuno, Y. Kuroda, A. Shimojima, H. Wada, and K. Kuroda, *Chem. Eur. J.*, **21**, 13073 (2015).
40. K.-M. Choi and K. Kuroda, *Chem. Commun.*, **47**, 10933 (2011).

41. Y. Kuroda and K. Kuroda, *Angew. Chem., Int. Ed.*, **122**, 7147 (2010).
42. A. Ohma, K. Shinohara, A. Iiyama, T. Yoshida, and A. Daimaru, *ECS Trans.*, **41(1)**, 775 (2011).
43. A. Lewera, L. Timperman, A. Roguska, and N. Alonso-Vante, *J. Phys. Chem. C*, **115**, 20153 (2011).
44. A. Dauscher, L. Hilaire, F. Le Normand, W. Müller, G. Maire, and A. Vasquez, *Surf. Interface Anal.*, **16**, 341 (1990).
45. A. S. Aricò, A. K. Shukla, H. Kim, S. Park, M. Min, and V. Antonucci, *Appl. Surf. Sci.*, **172**, 33 (2001).
46. T. Huizinga, H. v. T. Blik, J. Vis, and R. Prins, *Surf. Sci.*, **135**, 580 (1983).
47. E. I. Vovk, A. V. Kalinkin, M. Y. Smirnov, I. O. Klembovskii, and V. I. Bukhtiyarov, *J. Phys. Chem. C*, **121**, 17297 (2017).
48. S. Y. Moon, B. Naik, C.-H. Jung, K. Qadir, and J. Y. Park, *Catal. Today*, **265**, 245 (2016).
49. K. Qadir, S. H. Kim, S. M. Kim, H. Ha, and J. Y. Park, *J. Phys. Chem. C*, **116**, 24054 (2012).
50. B. Lim, M. Jiang, P. H. Camargo, E. C. Cho, J. Tao, X. Lu, Y. Zhu, and Y. Xia, *Science*, **324**, 1302 (2009).
51. L. Chevallier, A. Bauer, S. Cavaliere, R. Hui, J. Roziere, and D. J. Jones, *ACS Appl. Mater. Interfaces*, **4**, 1752 (2012).
52. L. Yang, J. Yu, Z. Wei, G. Li, L. Cao, W. Zhou, and S. Chen, *Nano Energy*, **41**, 772 (2017).
53. Y. Senoo, K. Taniguchi, K. Kakinuma, M. Uchida, H. Uchida, S. Deki, and M. Watanabe, *Electrochem. Commun.*, **51**, 37 (2015).
54. J.-E. Won, D.-H. Kwak, S.-B. Han, H.-S. Park, J.-Y. Park, K.-B. Ma, D.-H. Kim, and K.-W. Park, *J. Catal.*, **358**, 287 (2018).
55. K. Banno, M. Mizuno, K. Fujita, T. Kubo, M. Miyoshi, T. Egawa, and T. Soga, *Appl. Phys. Lett.*, **103**, 082112 (2013).
56. S. Tian, N. Tian, Z.-Y. Zhou, W.-F. Lin, and S.-G. Sun, *ACS Energy Lett.*, **8**, 1892 (2017).
57. E. Valenzuela, V. Ramos-Sanchez, A. A. Lambert Arista, and O. Savadogo, *J. Mater.*, **2013**, 706513 (2013).
58. D. Malevich, V. Drozdovich, and I. Zharskii, *Studies in Surface Science and Catalysis*, Elsevier, p. 359 (1997).
59. Z.-W. Wei, H.-J. Wang, C. Zhang, K. Xu, X.-L. Lu, and T.-B. Lu, *Angew. Chem., Int. Ed.*, **60**, 16622 (2021).
60. R. A. Armengol, J. Lim, M. Ledendecker, K. Hengge, and C. Scheu, *Nanoscale Adv.*, **3**, 5075 (2021).
61. K. Miyazawa, T. Nagai, K. Kimoto, M. Yoshitake, and Y. Tanaka, *Surf. Interface Anal.*, **52**, 23 (2020).
62. N. M. Marković, R. R. Adžić, B. Cahan, and E. Yeager, *J. Electroanal. Chem.*, **377**, 249 (1994).
63. A. E. Sleightholme and A. Kucernak, *Electrochim. Acta*, **56**, 4396 (2011).
64. M. Inaba, A. Zana, J. Quinson, F. Bizzotto, C. Dosche, A. Dworzak, M. Oezaslan, S. B. Simonsen, L. T. Kuhn, and M. Arenz, *ACS Catal.*, **11**, 7144 (2021).
65. B. E. Hayden, D. Pletcher, J.-P. Suchsland, and L. J. Williams, *Phys. Chem. Chem. Phys.*, **11**, 9141 (2009).
66. Na. Tian, Z.-Y. Zhou, and S.-G. Sun, *J. Phys. Chem. C*, **112**, 19801 (2008).
67. P. G. de Gennes, *Rev. Mod. Phys.*, **57**, 827 (1985).
68. N. S. Porter, H. Wu, Z. Quan, and J. Fang, *Acc. Chem. Res.*, **46**, 1867 (2013).
69. W. Nie, Q. Zhu, Y. Gao, Z. Wang, Y. Liu, X. Wang, R. Chen, F. Fan, and C. Li, *Nano Lett.*, **21**, 8901 (2021).